

Article

Laser Ablation Synthesis and Characterization of Tb₂O₃ Nanoparticles for Magneto-Optical Ceramics

Roman N. Maksimov ^{1,2,*} , Vladimir V. Osipov ¹, Garegin R. Karagedov ³, Vyacheslav V. Platonov ¹, Artem S. Yurovskikh ², Albert N. Orlov ¹, Alfiya V. Spirina ¹ and Vladislav A. Shitov ¹

¹ Institute of Electrophysics of the Ural Branch of the Russian Academy of Sciences, 106 Amundsen St., 620016 Ekaterinburg, Russia

² Ural Federal University Named after the First President of Russia B.N. Yeltsin, 19 Mira St., 620002 Ekaterinburg, Russia

³ Institute of Solid State Chemistry and Mechanochemistry of the Siberian Branch of the Russian Academy of Sciences, 18 Kutateladze St., 630128 Novosibirsk, Russia

* Correspondence: romanmaksimov@e1.ru; Tel.: +7-343-2678-779

Abstract: In this study, nano-sized individual Tb₂O₃ particles synthesized by the laser ablation method were extensively characterized and assessed as suitable precursors for the fabrication of transparent magneto-optical ceramics without requiring the introduction of grain growth inhibitors and stabilizing additives. The as-produced powder comprised 13 nm particles with a spherical shape and monoclinic crystal structure, whose full transformation into cubic phase was achieved after heating at 950 °C and 700 °C under vacuum and Ar gas, respectively. After subjecting the nanopowder compact to pre-sintering at 1350 °C, the microstructural features were investigated along with their correlation to the optical transmittance of Tb₂O₃ ceramic hot isostatically pressed (HIPed) for 2 h at 1450 °C under 200 MPa. The as-HIPed sample had a brownish color, with an optical transmittance of 65.3% at a wavelength of 1060 nm and an average grain size of 14 μm. The Verdet constant measured at wavelengths of 633 nm and 1060 nm was 471 rad T⁻¹ m⁻¹ and 142 rad T⁻¹ m⁻¹ to confirm a very high content of magneto-active Tb³⁺ ions. The obtained results indicate that laser ablation synthesis of nanoparticles followed by pre-sintering and HIP is a promising approach for the manufacture of magneto-optical Tb₂O₃ ceramics without specific sintering aids.

Keywords: terbium oxide; nanopowder; laser ablation; polymorphic phase transition; magnetic moment; densification; magneto-optical ceramic; Verdet constant



Citation: Maksimov, R.N.; Osipov, V.V.; Karagedov, G.R.; Platonov, V.V.; Yurovskikh, A.S.; Orlov, A.N.; Spirina, A.V.; Shitov, V.A. Laser Ablation Synthesis and Characterization of Tb₂O₃ Nanoparticles for Magneto-Optical Ceramics. *Inorganics* **2022**, *10*, 173. <https://doi.org/10.3390/inorganics10100173>

Academic Editor: Sergey Kuznetsov

Received: 10 September 2022

Accepted: 12 October 2022

Published: 18 October 2022

Publisher's Note: MDPI stays neutral with regard to jurisdictional claims in published maps and institutional affiliations.



Copyright: © 2022 by the authors. Licensee MDPI, Basel, Switzerland. This article is an open access article distributed under the terms and conditions of the Creative Commons Attribution (CC BY) license (<https://creativecommons.org/licenses/by/4.0/>).

1. Introduction

Recently, single- and polycrystalline materials based on terbium sesquioxide (Tb₂O₃) have attracted the interest of researchers as a promising magneto-optical medium for Faraday isolators owing to extremely high content of active Tb³⁺ ions in a bixbyite structure (~2.59 × 10²² cm⁻³) [1–3]. In 2015, Veber et al. presented the first successful flux growth of several mm-sized cubic Tb₂O₃ crystals, which demonstrated a Verdet constant (134 rad T⁻¹ m⁻¹) at least three times higher than that of Tb₃Ga₅O₁₂ crystals used in commercial Faraday rotators [4]. A short time later, it was shown that ceramic technology used for manufacturing Tb₂O₃ materials offers several important advantages over crystal growth methods including larger sizes and better optical performance [5,6].

When preparing transparent ceramics, one of the main challenges involves the achievement of full densification at reasonably low temperatures. At a temperature of 1550 °C, Tb₂O₃ undergoes polymorphic phase transformation from cubic to monoclinic structure, resulting in sample fracture [7–9]. Although isovalent additives of yttrium or lutetium sesquioxides can be used to stabilize cubic modification at higher temperatures [10,11], they lead to a deterioration of thermal and magnetic properties due to lattice distortion and a concomitant decrease in the content of Tb³⁺ ions. Aliovalent grain-growth inhibiting

additives of zirconia can be additionally utilized for improving optical quality due to the formation of a solid solution, which prevents pores breaking away from grain boundaries [5,6,12,13]. However, the abovementioned sintering additives are undesirable for the processing of advanced oxide ceramics for photonic applications due to their adverse effect on designated performances [14–18].

Thus, ultrafine Tb_2O_3 powders yielding an almost fully densified material without abnormal grain growth are highly demanded for modern ceramic technology. To date, a number of wet chemistry methods such self-propagating high-temperature synthesis and co-precipitation followed by the thermal decomposition of various precursors have been developed for the synthesis of terbium oxide powders having various morphologies and a primary particle size ranging from several tens of nanometers to about 135 nm [7,13,19–21]. Nevertheless, these powders feature insufficient densification below 1500 °C due to the presence of hard agglomerates, implying the utilization of ZrO_2 as a grain growth inhibitor for high temperature sintering. In this regard, laser ablation synthesis is a suitable method for producing Tb_2O_3 powders whose loosely aggregated particles have a characteristic size of about 15 nm ensuring their excellent sinterability [22,23]. In an earlier study [24], the laser ablation method was used for the synthesis of Yb-doped Lu_2O_3 nanopowder and ceramic samples with lasing quality at a final temperature as low as 1400 °C.

In the present study, we investigate the properties of Tb_2O_3 nanoparticles produced by the laser ablation method along with the possibility of fabricating transparent ceramics without sintering additives using a combination of pressureless densification and hot isostatic pressing.

2. Results and Discussion

2.1. Properties of Tb_2O_3 Nanoparticles

Figure 1 shows a TEM image of Tb_2O_3 nanopowder synthesized by the laser ablation method with the corresponding particle size distribution histogram presented in the inset. It is evident that the sample mainly consists of ultrafine, loosely aggregated and almost spherical-shaped particles with an average size of 13 nm. The Brunauer-Emmett-Teller (BET) surface area was determined to be 40.2 m²/g, corresponding to an equivalent particle diameter of 17 nm.

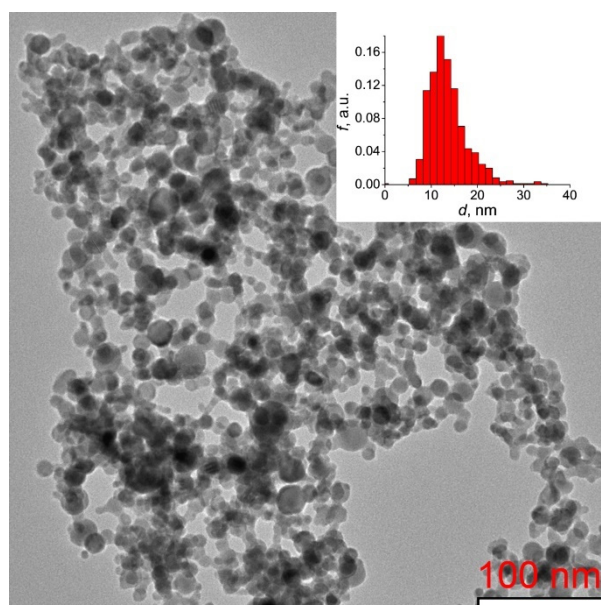


Figure 1. TEM image of Tb_2O_3 nanopowder synthesized by the laser ablation method. The inset presents the histogram of particle size distribution.

Powder X-ray diffractograms were collected to identify the crystal structure of the as-obtained Tb_2O_3 nanoparticles and their phase evolution during increase in temperature under vacuum (Figure 2). Positions and relative intensities of the diffraction peaks registered at 50 °C were found to be consistent with monoclinic B-type Tb_2O_3 (space group $C2/m$) referenced in ICDD PDF No. 01-074-2131. No recognizable traces of other crystalline phases specific to the Tb–O system [25,26] were detected within the typical experimental error (~ 2 wt.%). The lattice parameters determined from the Rietveld refinement ($a = 14.068$ Å, $b = 3.547$ Å, $c = 8.723$ Å, $\beta = 100.2^\circ$) were close to the standard values, confirming the phase purity of the synthesized Tb_2O_3 nanoparticles. The crystallite size calculated using the Debye–Scherrer equation was 13 nm, which was in full accordance with the average particle size obtained from TEM observations. It is interesting to note that two crystalline phases—namely, triclinic $\text{Tb}_{11}\text{O}_{20}$ (86 wt.%, ICDD PDF No. 03-065-4511) and cubic $\text{TbO}_{1.81}$ (14 wt.%, ICDD PDF No. 01-075-0275)—were identified in the initial target material.

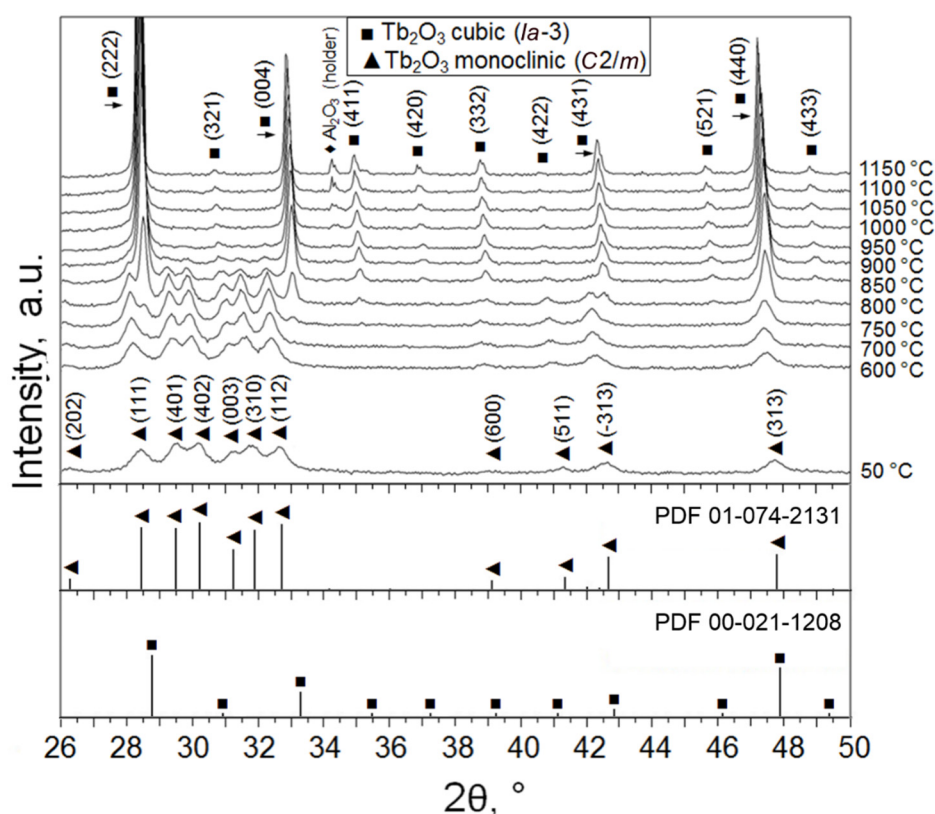


Figure 2. X-ray diffractogram showing the phase evolution of the obtained Tb_2O_3 nanopowder during heating up from 50 °C to 1150 °C under vacuum.

When the obtained nanoparticles are heated to 750 °C under vacuum (Figure 2), diffraction peaks additional to the characteristic peaks of the monoclinic phase begin to clearly appear at diffraction angles $2\theta \approx 28.3^\circ$, 32.8° , 34.9° and 37.1° , corresponding to the planes (2 2 2), (0 0 4), (4 1 1) and (4 0 2) of the cubic C-modification of Tb_2O_3 (space group $Ia-3$). In the temperature range 750–900 °C, two phases were simultaneously observed in the nanopowder; at 950 °C, a complete B \rightarrow C transformation occurred. Upon cooling down to room temperature, the sample showed only a monotonic change in the period of cubic lattice due to thermal compression.

The thermal behavior of the produced nanopowder in neutral (Ar gas) medium and air was investigated using the thermogravimetric (TG) and differential thermal analyses (DTA). When the sample is heated in Ar, the DTA curve (Figure 3a) shows a series of endothermic processes corresponding to water evaporation and a broad exothermic peak of organic

burnout near 340 °C. These reactions resulted in a rapid weight loss of 7.1%, with total weight loss reaching 8.4% at 1300 °C. The next exothermic peak with a maximum at 674 °C appears to be associated with the phase transformation of the monoclinic phase to the cubic phase of Tb₂O₃, which was retained in the sample after cooling to room temperature. In turn, a number of overlapping endothermic processes also appear in the temperature range of 20–350 °C when the produced nanopowder is heated in air (Figure 3b), of which the first (at 139 °C) and last (at 327 °C) peaks can be clearly distinguished. In this region, the weight loss reached 4.7%. Next, an exothermic peak is observed; in contrast to the experiment carried out under argon, this is accompanied by an 0.3% increase in the sample mass, which is probably due to the oxidation of terbium sesquioxide to TbO_{1.81}. Then, in the temperature ranges of 500–600 °C and 870–940 °C, two endothermic peaks with maxima at 573 °C and 913 °C are detected, indicating a two-stage reduction of the sample to a stoichiometry close to Tb₂O₃. On the TG curve, these processes become apparent as a sharp decrease in the sample mass. Upon cooling, however, the powder again oxidized, as demonstrated by the two crystalline phases of Tb₁₁O₂₀ and TbO_{1.81} identified at room temperature using X-ray diffraction analysis (not shown here).

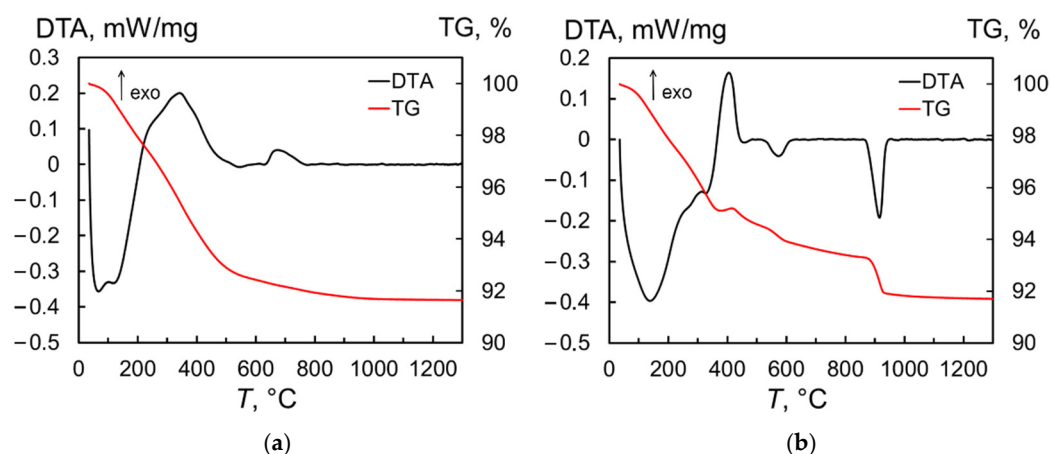


Figure 3. Derivatograms of Tb₂O₃ nanopowder heated in argon (a) and air (b).

XPS technique was used to explore the valence state of terbium at the particles' surface. The Tb 4d core level XPS spectrum (Figure 4a) shows a main peak at 151 eV accompanied with a weak shoulder above 155 eV, which is usually assigned to 4d states of tetravalent terbium [27–29]. The next broad peak at 178 eV is attributed to charge-transfer satellite [30]. The XPS spectrum of the most intense Tb 3d core level (Figure 4b) consists of two principal Tb 3d_{3/2} and Tb 3d_{5/2} photoemission bands with the maxima at 1277 eV and 1242 eV, respectively. The latter is followed by a relatively strong satellite in the range 1250–1255 eV specific to Tb⁴⁺: this feature is not observed in non-oxide compounds formed by Tb³⁺ ions [31,32]. Thus, these findings confirm the presence of Tb in both valence states at the surface of nanoparticles. However, it was not possible to estimate the Tb³⁺/Tb⁴⁺ molar ratio using deconvolution of the Tb 4d or Tb 3d spectra due to a lack of well-determined reference spectra from pure and stoichiometric Tb₂O₃/TbO₂ surfaces.

Reliable estimation of Tb³⁺/Tb⁴⁺ contents and degree of oxidation was obtained in the process of investigating the magnetic properties of the as-produced nanoparticles. For this purpose, magnetization values measured in the range 2–300 K were used to calculate the temperature dependence of the molar magnetic susceptibility according to the following equation [33]:

$$\chi_M = \frac{MM_r}{Hmn} \quad (1)$$

where M—measured magnetization; M_r—molar mass of terbium sesquioxide (365.85 g/mol); H—magnetic field strength (500 Oe); m—sample mass taking into account the content of volatile species (8.4 wt.% from TG analysis); n—number of magnetic ions per formula unit

(for Tb_2O_3 $n = 2$). By fitting of the inverse magnetic susceptibilities in the paramagnetic region (50–300 K, Figure 5) to the Curie–Weiss law, we extracted the Curie–Weiss constant $\theta_{\text{CW}} = -13.1$ K and the Curie constant $C = 11.2$ K emu/(mol Oe). A comparable Curie constant value was previously found in the terbium oxide powder calcined for 2 h at a temperature of 900 °C in a hydrogen atmosphere [34]. The effective magnetic moment per paramagnetic center calculated by the formula $\mu_{\text{eff}} = 2.828\sqrt{C} = 9.47 \mu_{\text{B}}$ is slightly lower than the theoretical magnetic moment $\mu_{\text{calc}} = 9.72 \mu_{\text{B}}$ predicted by Hund’s rule for the free Tb^{3+} ion, suggesting the presence of tetravalent Tb. The respective fractions of Tb^{3+} and Tb^{4+} cations can be estimated the formula $\mu_{\text{eff}}^2 = x\mu_{\text{Tb}^{3+}}^2 + (1-x)\mu_{\text{Tb}^{4+}}^2$, where x corresponds to the fraction of trivalent terbium and $(1-x)$ to that of tetravalent terbium constituting the particles; $\mu_{\text{Tb}^{3+}}$ and $\mu_{\text{Tb}^{4+}}$ refer to the theoretical effective moments of these ions. According to the calculations, the contents of Tb^{3+} and Tb^{4+} in the as-synthesized nanopowder are 84.7 at.% and 15.3 at.%, respectively, resulting in an estimative oxygen stoichiometry $\text{TbO}_{1.58}$.

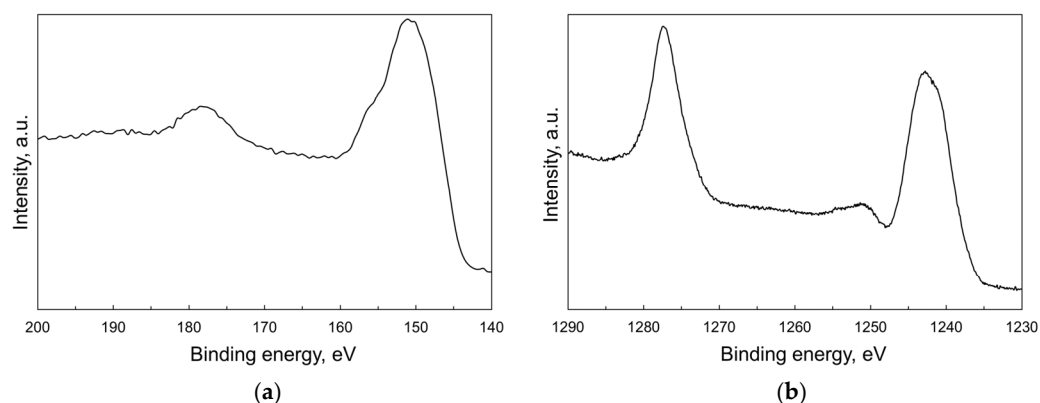


Figure 4. XPS spectra corresponding to 4d (a) and 3d (b) core levels for the as-synthesized Tb_2O_3 nanoparticles.

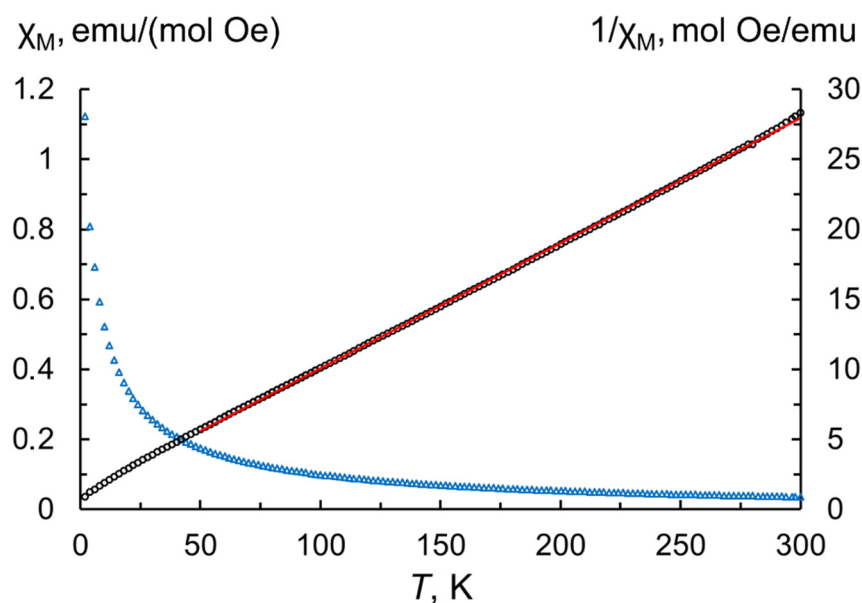


Figure 5. Temperature dependences of molar magnetic susceptibility (blue triangles) and inverse molar magnetic susceptibility (black circles) at 500 Oe for the as-synthesized Tb_2O_3 nanoparticles. The solid red line represents the Curie–Weiss fit.

The reduction in terbium oxide nanoparticles from the target material having an approximate composition of $\text{TbO}_{1.82}$ during laser ablation synthesis in air flow can be

explained as follows. Intense evaporation of terbium oxide under the action of laser pulses with a duration of $>1 \mu\text{s}$ occurs from a molten pool formed on the surface of the target at a temperature close to boiling point. Following laser radiation on a specific area of the target, the melt cools down too quickly for its oxidation to occur. Therefore, the chemical composition of this area at the surface during the subsequent evaporation cycle will differ from the initial composition. Here, it appears that vapors consisting of TbO, Tb and oxygen are produced, regardless of the O/Tb ratio in the initial target. As a result of the condensation of these vapors, the first nanoparticles having a composition close to Tb_2O_3 are formed; these can then be oxidized to some extent depending on the oxygen partial pressure in the laser plume and evaporation chamber.

In order to identify the pre-sintering temperatures suitable for post-HIP treatment, the densification behavior of the obtained nanoparticles under vacuum was investigated. Figure 6 presents density versus temperature for Tb_2O_3 nanopowder compact heated up to $1450 \text{ }^\circ\text{C}$ in a dilatometer at $3 \text{ }^\circ\text{C}/\text{min}$. Remarkably, the sample featured a linear shrinkage even at relatively low temperatures ($<600 \text{ }^\circ\text{C}$). A notable increase in density is observed in the range $620\text{--}840 \text{ }^\circ\text{C}$ and the densification rate reached the first maximum of $-0.2 \times 10^{-3} \text{ min}^{-1}$ at $700 \text{ }^\circ\text{C}$. At the next temperature range of $840\text{--}990 \text{ }^\circ\text{C}$, the densification curve showed an inflection attributable to the monoclinic-to-cubic phase transformation. This phase conversion results in an almost threefold increase in the volume of unit cell. Indeed, the observed inflection reflects the development of two competitive processes namely temperature-related shrinkage and phase-transformation-assisted expansion. The densification rate decreases from the first maximum to reach a local minimum at $900 \text{ }^\circ\text{C}$. When the phase conversion is complete, the shrinkage rate grows towards the second peak near $1100 \text{ }^\circ\text{C}$, at which temperature the density of sintered sample attained $5.84 \text{ g}/\text{cm}^3$. With a further increase in temperature up to $1450 \text{ }^\circ\text{C}$, the density monotonically reaches $7.43 \text{ g}/\text{cm}^3$ corresponding to a relative density of 94.5% with respect to cubic Tb_2O_3 ($\rho = 7.86 \text{ g}/\text{cm}^3$). Thus, Tb_2O_3 nanoparticles obtained by laser ablation have better sinterability as compared with the ultrafine terbium oxide powder produced by the self-propagating high-temperature synthesis [35], whose densification was demonstrated up to $6.475 \text{ g}/\text{cm}^3$ ($\rho_{\text{rel}} = 82\%$) at $1450 \text{ }^\circ\text{C}$.

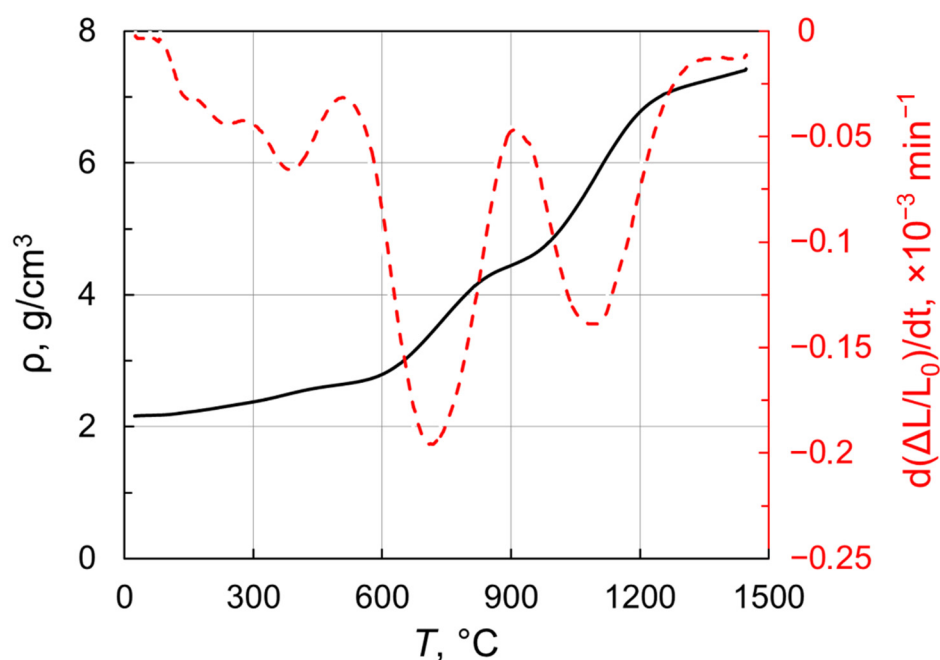


Figure 6. Density and shrinkage rate versus temperature for Tb_2O_3 nanopowder compact.

2.2. Characterization of the as-HIPed Tb_2O_3 Transparent Ceramics

Figure 7a shows the transmission spectra of the as-fabricated Tb_2O_3 ceramic. The optical transmittance at a wavelength of 1060 nm reached 65.3%. Using the refractive index value $n = 1.94$ reported by Ikesue et al. [5] with the modified Fresnel equation $T = 2n/(n^2 + 1)$ and taking into account multiple light reflections at the sample interfaces, we calculated the theoretical transmission of Tb_2O_3 as 81.5% near 1 μm . Consequently, the optical quality of the obtained ceramic should be significantly improved to permit their utilization as magneto-active media for Faraday isolators. A broad absorption feature is clearly observed in the range 400–550 nm, which is attributed to the $4f \rightarrow 5d_1$ optical transition of trivalent cerium [12] present in the raw powder as an accidental impurity (see Section 3.1). In addition, a dark coloration of the sample (Figure 7b) and drop-off in transmittance in the visible and near-IR spectral ranges suggest the presence of absorption centers such as oxygen vacancies and Tb^{2+} cations formed during HIP treatment in a graphite furnace. A certain number of spherical-shaped pores of 2–5 μm diameter were detected using an optical microscope. The average volume of pores was evaluated to be 25.8 ppm. These scattering centers, which were homogeneously distributed through the depth of the sample (inset of Figure 7a), constitute another reason for the decrease in transmission. It is most likely that the formation of large pores having sizes comparable to that of grains (see below) originates from the non-uniform particle packing and underdeveloped processing conditions. By improving the powder pressing and sintering techniques, it should be possible to significantly decrease the content of scattering centers in the fabricated Tb_2O_3 ceramic.

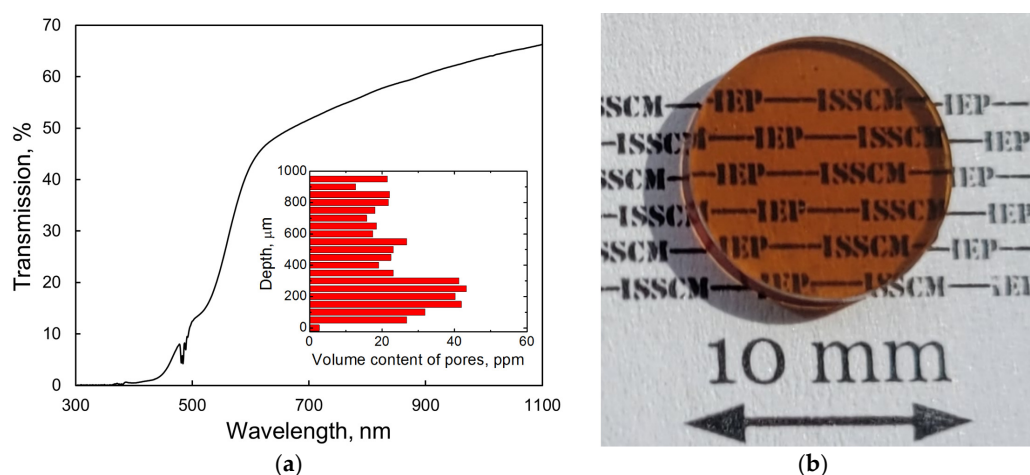


Figure 7. Transmission spectrum (a) and photograph (b) of the as-HIPed Tb_2O_3 ceramic with a thickness of 1.5 mm.

Several approaches can be used in the processing of transparent ceramics to prevent formation of color centers related to oxygen stoichiometry. For example, furnaces equipped with tungsten and molybdenum components are more suitable for the HIP stage as compared with graphite, which produces a strongly reductive atmosphere when heated. Moreover, pre-sintered samples can be encapsulated using various materials acting as a diffusion barrier (Pt, Mo or Ta foils) [36–39] to effectively avoid unwanted contamination. In case color centers related to Tb^{4+} cations exist in the produced material, post-annealing in a reducing atmosphere is advantageous for the $Tb^{4+} \rightarrow Tb^{3+}$ conversion in order to enable the preparation of colorless samples [40].

The Raman spectrum taken from the nanopowder with the monoclinic phase is shown in Figure 8 along with the as-HIPed cubic Tb_2O_3 ceramic sample. The positions of the measured Raman modes for the nanoparticles (81, 94, 108, 122, 163, 214, 264, 307, 368, 390, 423, 447, 492 and 598 cm^{-1}) coincide well with results presented elsewhere [41,42]. The additional intense modes appearing in the extended region at 607 cm^{-1} and 631 cm^{-1} are also likely to belong to the phonons of the monoclinic lattice. Furthermore, a prominent

peak at 1084 cm^{-1} and small diffuse band centered at 1300 cm^{-1} can be observed. The nature of these vibrational modes can be associated with CO_3^{2-} [43] and vibrations of structural complexes formed by a Tb atom and the nearest oxygen atom in the monoclinic structure. Taking the instrumental error into account, the observed Raman active modes of the ceramic sample ($93, 117, 132, 144, 322, 366, 451$ and 576 cm^{-1}) match the corresponding spectrum of cubic Tb_2O_3 single crystal [41]. In addition to the characteristic modes of the cubic lattice, several peaks attributed to the local vibrational modes were observed [41,42]. In the Raman spectrum of the as-HIPed ceramic sample, we also observed one pronounced peak at 214 cm^{-1} ; however, this belongs to the local vibrational mode and not to the vibrations of the main lattice. The absence of carbon contamination was confirmed by the absence of characteristic peaks at 1350 cm^{-1} and 1600 cm^{-1} related to the D- and G-bands of C, respectively.

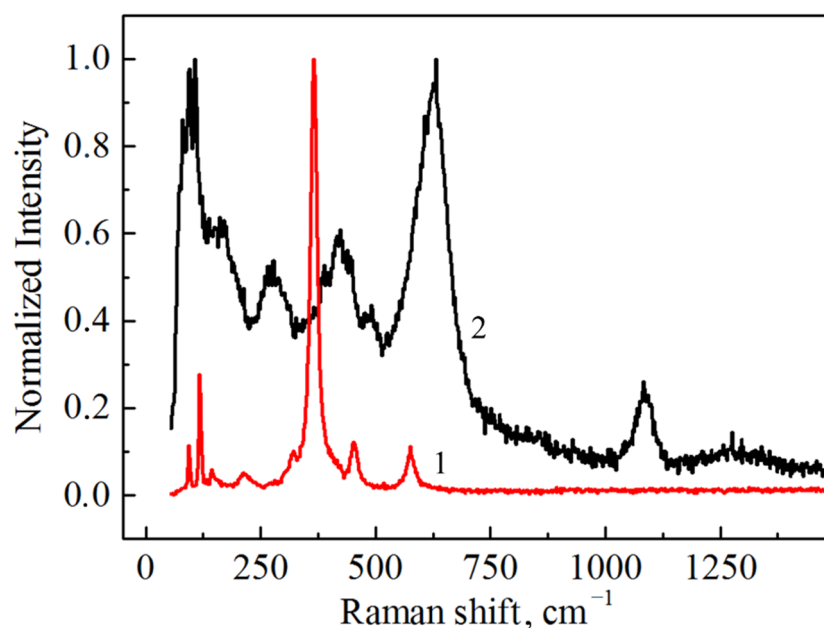


Figure 8. Raman spectra of the as-obtained Tb_2O_3 ceramic (1) and nanopowder (2).

The characteristic microstructures of Tb_2O_3 ceramics both before and after HIP treatment are shown in Figure 9. The pre-sintered sample shows submicrometer-grained structure with an average grain size of $0.74\text{ }\mu\text{m}$. The average grain size after HIP treatment increased to $14\text{ }\mu\text{m}$, which is much larger than that of Tb_2O_3 ceramics fabricated at higher temperatures using zirconium as a grain growth inhibitor [5,12,13]. Due to enhanced grain growth during HIP treatment at $1450\text{ }^\circ\text{C}$, the pores were not eliminated having become intragranular.

The Verdet constant of the as-obtained Tb_2O_3 ceramic was measured at the wavelengths of 633 nm and 1060 nm . A terbium gallium garnet (TGG) single crystal was used as a reference sample. Under the magnetic field strength of 0.28 T , the rotation angle at the wavelength of 633 nm was $12^\circ 1'$ and $6^\circ 20'$ corresponding to the Verdet constant of $471\text{ rad T}^{-1}\text{ m}^{-1}$ and $138\text{ rad T}^{-1}\text{ m}^{-1}$ for Tb_2O_3 ceramic and TGG crystal, respectively. At the wavelength of 1060 nm , the Verdet constant was determined to be $142\text{ rad T}^{-1}\text{ m}^{-1}$ and $41\text{ rad T}^{-1}\text{ m}^{-1}$, respectively. The obtained values for the TGG crystal are consistent with literature data considering the relative measurement error of 5% [44]. The Verdet constant of the fabricated Tb_2O_3 ceramic is practically equivalent to that of high-purity Tb_2O_3 crystal grown by the flux method [4], indicating negligible content of detrimental Tb^{4+} ions. These measurements confirm our assumption that the dark coloration of the sample HIPed in a graphite furnace is caused by the color centers and not by the presence of tetravalent terbium.

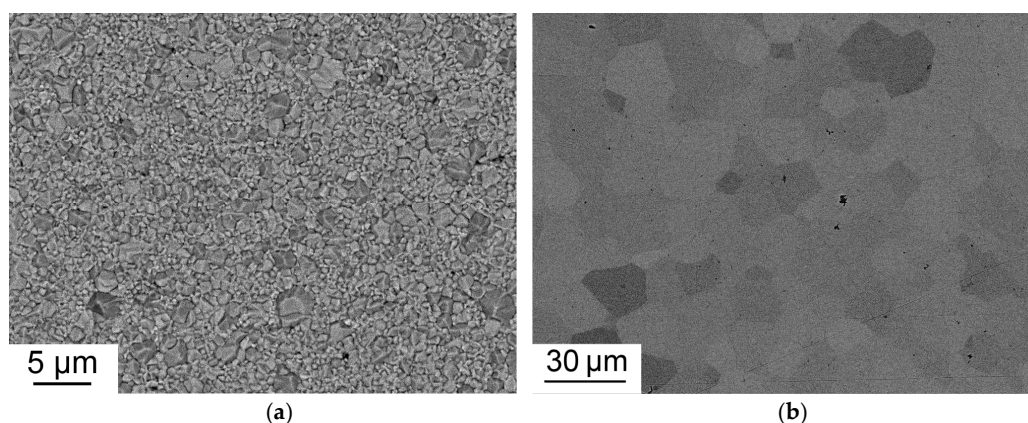


Figure 9. Microstructure of Tb_2O_3 ceramic pre-sintered at $1350\text{ }^\circ\text{C}$ (a) and after HIP treatment at $1450\text{ }^\circ\text{C}$ (b).

3. Materials and Methods

3.1. Synthesis of Nanopowder

Terbium oxide nanoparticles were produced by the laser ablation method comprising evaporation of a solid target material using laser radiation with an eventual condensation of vapors carried out in air flow. In order to prepare the target for ablation, coarse raw powder (Tb_4O_7 , $Tb/(\text{Total rare earth metals}) = 99.99\%$, Lanhit Company, Moscow, Russia) having a specific surface area of $1.2\text{ m}^2/\text{g}$ was uniaxially dry-pressed at 20 MPa to form a cylindrical green body of 65 mm diameter and 25 mm height, which was then pre-sintered at $1250\text{ }^\circ\text{C}$ for 5 h in air. The impurity composition of the raw powder according to the vendor's certificate is reported in Table 1.

Table 1. Impurity composition of raw terbium oxide powder.

Composition	Main Impurities										
	Al	Si	Ca	Ti	Fe	Zn	Ce	Nd	Gd	Dy	Yb
Content, ppm	2	10	3	5	10	2	50	7	4	5	3

Ablation of the obtained target was conducted using an LS-07N ytterbium fiber laser (IRE-Polus, Fryazino, Russia), whose radiation was focused on the target's surface placed inside an evaporation chamber. During the synthesis of nanopowder, the laser generated rectangular pulses of $120\text{ }\mu\text{s}$ duration at 1070 nm with a duty factor of 2 and at a peak power of 600 W. For uniform wear of the surface, the target was rotated and moved in the horizontal direction; following evaporation of the surface layer, it was lifted vertically. The resulting vapor phase was conducted into an air flow of atmospheric pressure, in which it was cooled to condense and crystallize in the form of nano-sized particles. After extracting the largest droplets and fragments of the target using a cyclone system, the nanopowder was collected in bag filter. The detailed description of our experimental setup and main laser parameters during the ablation process can be found elsewhere [23].

3.2. Fabrication of Tb_2O_3 Ceramic

Transparent Tb_2O_3 ceramic was fabricated by pressureless densification under vacuum followed by a capsule-free hot isostatic pressing (HIP). Sintering additives were not introduced during the processing steps. The nanoparticles synthesized by the laser ablation method were uniaxially pressed at 50 MPa into green body of 14 mm diameter and then pre-sintered at $1350\text{ }^\circ\text{C}$ for 1 h under the residual gas pressure of 10^{-4} Pa . The $B \rightarrow C$ phase conversion occurred in the powder compact during sintering process. The relative density of the sample at this stage was 97.3% with respect to the theoretical density of cubic Tb_2O_3 (7.82 g/cm^3). Subsequent consolidation to the nearly fully dense transparent ceramic was

achieved at a temperature of 1450 °C for 2 h under argon gas at a pressure of 200 MPa using an AIP6-30H HIP (American Isostatic Presses, Columbus, OH, USA) equipped with a graphite furnace. The final thickness of the as-HIPed ceramic sample after polishing was 1.5 mm.

3.3. Characterization Methods

The morphology of the as-synthesized terbium oxide nanopowder was studied using a JEM 2100 (TEM, JEOL Ltd., Tokyo, Japan) transmission electron microscope. The obtained TEM micrographs were used to measure the equivalent diameter of at least 800 particles for plotting their size distribution. The specific surface area of the nanopowder was measured by the Brunauer-Emmett-Teller (BET) method with a TriStar 3000 gas adsorption analyzer (Micromeritics, Norcross, GA, USA). In order to determine the processes occurring during the thermal treatment of nanoparticles under various media (vacuum, argon or air), TG/DTA and high-temperature X-ray diffraction analyzes were carried out using a Diamond TG-DTA derivatograph (PerkinElmer, Waltham, MA, USA) and a D8 Advance diffractometer (Bruker AXS, Karlsruhe, Germany) equipped with an Anton Paar HTK 1200N high temperature chamber, respectively. The X-ray photoelectron spectrum of the as-synthesized nanoparticles was recorded using a K-Alpha+ spectrometer (Thermo Fisher Scientific, Waltham, MA, USA). The magnetic characteristics of the nanopowder were studied in a temperature range of 2–300 K at a magnetic field strength of 500 Oe using an MPMS-XL-7 EC SQUID magnetometer (Quantum Design, San Diego, CA, USA). The sintering densification curve of the nanopowder compacted at a pressure of 50 MPa into a cylinder of 8 mm diameter and 5.2 mm height was recorded by heating up the sample to 1450 °C at a rate of 3 °C/min under a residual gas pressure of 0.4 Pa using a DIL 402 C horizontal dilatometer (NETZSCH, Selb, Germany).

The microstructure of the polished surfaces of the ceramics both before and after HIP treatment was observed using a scanning electron microscope Mira LMS (Tescan, Brno, Czech Republic). In order to reveal the grain structure, the polished surfaces were chemically etched by placing the samples in nitric acid for 5 min at room temperature. The average content of scattering centers throughout the depth of the sample was estimated by means of the direct count method using an optical microscope BX51TRF (Olympus Corp., Tokyo, Japan). The transmission spectrum of the as-HIPed Tb₂O₃ ceramic was measured over a wavelength range of 200–1100 nm using a UV-1700 spectrophotometer (Shimadzu Corp., Kyoto, Japan).

The experimental setup for the Verdet constant measurements is schematically shown in Figure 10. Radiation from a He-Ne or diode-pumped Nd:YAG lasers (1) modulated by the rotating shutter (2) at a frequency of 1515 Hz and linearly polarized by a Glan-Taylor prism (3) falls on the sample under test (4) placed between two permanent Nd-magnets (5) having a 3 mm diameter hole. Furthermore, the laser radiation is propagated through the output Glan-Taylor prism (6) and then recorded by a FD-24K photodiode (7). Electrical signals from the photodetector are fed to a Tektronix TDS5034B oscillograph (8). The magnetic field strength between two Nd-magnets was measured using a NOVOTEST MF-1 magnetometer. During the magnetic field sweep, the Faraday rotation of the sample was compensated by the reverse rotation of the output Glan-Taylor prism (analyzer) until zero light intensity. Measurement of the rotation angle of the polarization plane was conducted using the limb of the analyzer. The rotation angle measurement error was approximately 2–3 arcmin. The relative error of the Verdet constant determination was 5%.

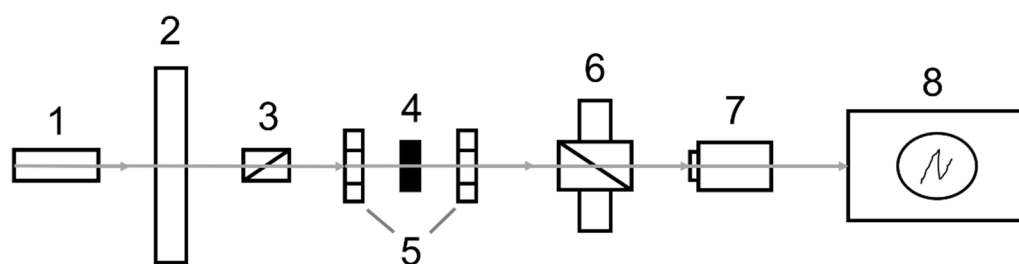


Figure 10. Block-scheme of experimental set-up used for Verdet constant measurement.

4. Conclusions

Nano-sized individual Tb_2O_3 nanoparticles exhibiting spherical morphology and an average size of 13 nm were synthesized using a laser ablation method. This involved evaporating a solid target material using Yb-fiber laser with the eventual condensation of the vapor carried out in air flow. According to the results of high-temperature XRD and TG/DTA analyses, the monoclinic crystal structure of the obtained particles can be irreversibly modified into a cubic structure by heat treatment under vacuum or Ar gas. From the magnetic measurements, we determined the values of the Curie–Weiss constant $\theta_{\text{CW}} = -13.1$ K, the Curie constant $C = 11.2$ K emu/(mol Oe) and the effective magnetic moment per paramagnetic center $\mu_{\text{eff}} = 9.47 \mu_{\text{B}}$ indicating the existence of both Tb^{3+} and Tb^{4+} ions in the as-synthesized nanopowder. Transparent Tb_2O_3 ceramic exhibiting an optical transmittance of 65.3% at a wavelength of 1060 nm, an average grain size of 14 μm and a scattering centers volume of 25.8 ppm was fabricated by a combination of pre-sintering for 1 h at 1350 $^\circ\text{C}$ under vacuum and hot isostatic pressing for 2 h at 1450 $^\circ\text{C}$ under 200 MPa of Ar gas pressure. Despite the brownish coloration of the as-HIPed sample, the Verdet constant at a wavelength of 1060 nm was measured to be 471 $\text{rad T}^{-1} \text{m}^{-1}$, suggesting the presence of color centers irrelevant to tetravalent terbium. Once the processing conditions for eliminating residual pores and absorption centers are determined, fabrication of a sintering aid free transparent Tb_2O_3 ceramic with advanced magneto- and thermo-optical performances will be possible using laser ablation synthesis followed by a sintering plus HIP approach.

Author Contributions: Conceptualization, R.N.M. and V.A.S.; Funding acquisition, R.N.M.; Investigation, R.N.M., A.S.Y., A.N.O. and A.V.S.; Methodology, G.R.K. and A.N.O.; Project administration, R.N.M.; Resources, G.R.K. and V.V.P.; Writing—original draft, R.N.M. and V.A.S.; Writing—review and editing, V.V.O. All authors have read and agreed to the published version of the manuscript.

Funding: This research was funded by the Russian Science Foundation, grant number 22-23-00658, <https://rscf.ru/en/project/22-23-00658/> (accessed on 10 September 2022).

Institutional Review Board Statement: Not applicable.

Informed Consent Statement: Not applicable.

Data Availability Statement: Not applicable.

Acknowledgments: The authors are grateful to the “Geoanalitik” shared research facilities of the IGG UB RAS for support with sample polishing (D.A. Zamyatin, N.S. Chebykin) and SEM (G.B. Mikhalevsky). The re-equipment and comprehensive development of the “Geoanalitik” shared research facilities of the IGG UB RAS is supported by the Ministry of Science and Higher Education of the Russian Federation (Agreement No. 075-15-2021-680).

Conflicts of Interest: The authors declare no conflict of interest.

References

1. Carothers, K.J.; Norwood, R.A.; Pyun, J. High Verdet constant materials for magneto-optical Faraday rotation: A Review. *Chem. Mater.* **2022**, *34*, 2531–2544. [CrossRef]
2. Vojna, D.; Slezak, O.; Lucianetti, A.; Mocek, T. Verdet constant of magneto-active materials developed for high-power Faraday devices. *Appl. Sci.* **2019**, *9*, 3160. [CrossRef]

3. Dai, J.; Li, J. Promising magneto-optical ceramics for high power Faraday isolators. *Scr. Mater.* **2018**, *155*, 78–84. [[CrossRef](#)]
4. Veber, P.; Velazquez, M.; Gadret, G.; Rytz, D.; Peltz, M.; Decourt, R. Flux growth at 1230 °C of cubic Tb₂O₃ single crystals and characterization of their optical and magnetic properties. *CrystEngComm* **2015**, *17*, 492–497. [[CrossRef](#)]
5. Ikesue, A.; Aung, Y.L.; Makikawa, S.; Yahagi, A. Polycrystalline (Tb_xY_{1-x})₂O₃ Faraday rotator. *Opt. Lett.* **2017**, *42*, 4399–4401. [[CrossRef](#)]
6. Ikesue, A.; Aung, Y.L.; Makikawa, S.; Yahagi, A. Total performance of magneto-optical ceramics with a bixbyite structure. *Materials* **2019**, *12*, 421. [[CrossRef](#)]
7. Balabanov, S.S.; Permin, D.A.; Rostokina, E.Y.; Egorov, S.V.; Sorokin, A.A.; Kuznetsov, D.D. Synthesis and structural characterization of ultrafine terbium oxide powders. *Ceram. Int.* **2017**, *43*, 16569–16574. [[CrossRef](#)]
8. Zinkevich, M. Thermodynamics of rare earth sesquioxides. *Prog. Mater. Sci.* **2007**, *52*, 597–647. [[CrossRef](#)]
9. Zhang, J.; Chen, H.; Wang, J.; Wang, D.; Han, D.; Zhang, J.; Wang, S. Phase transformation process of Tb₂O₃ at elevated temperatures. *Scr. Mater.* **2019**, *171*, 108–111. [[CrossRef](#)]
10. Yang, M.; Zhou, D.; Xu, J.; Tian, T.; Jia, R.; Wang, Z. Fabrication and magneto-optical property of yttria stabilized Tb₂O₃ transparent ceramics. *J. Eur. Ceram. Soc.* **2019**, *39*, 5005–5009. [[CrossRef](#)]
11. Zhang, J.; Chen, H.; Wang, J.; Wang, D.; Han, D.; Zhang, J.; Wang, S. Preparation of (Tb_{1-x}Lu_x)₂O₃ transparent ceramics by solid solution for magneto-optical application. *J. Eur. Ceram. Soc.* **2021**, *41*, 2818–2825. [[CrossRef](#)]
12. Balabanov, S.S.; Permin, D.A.; Rostokina, E.Y.; Palashov, O.V.; Snetkov, I.L. Characterizations of REE:Tb₂O₃ magneto-optical ceramics. *Phys. Status Solidi B* **2020**, *257*, 1900474. [[CrossRef](#)]
13. Hu, D.; Li, X.; Zhang, L.; Snetkov, I.; Chen, P.; Dai, Z.; Balabanov, S.; Palashov, O.; Li, J. Terbium (III) oxide (Tb₂O₃) transparent ceramics by two-step sintering from precipitated powder. *Magnetochemistry* **2022**, *8*, 73. [[CrossRef](#)]
14. Li, Q.; Wang, J.; Ma, J.; Ni, M.; Yang, F.; Liu, P.; Lee, K.Y.; Hsiang, H.-I.; Shen, D.; Tang, D. Fabrication of high-efficiency Yb:Y₂O₃ laser ceramics without photodarkening. *J. Am. Ceram. Soc.* **2022**, *105*, 3375–3381. [[CrossRef](#)]
15. Yin, D.; Ma, J.; Liu, P.; Yao, B.; Wang, J.; Dong, Z.; Kong, L.B.; Tang, D. Submicron-grained Yb:Lu₂O₃ transparent ceramics with lasing quality. *J. Am. Ceram. Soc.* **2019**, *102*, 2587–2592. [[CrossRef](#)]
16. Ikesue, A.; Aung, Y.L. Synthesis of Yb:YAG ceramics without sintering additives and their performance. *J. Am. Ceram. Soc.* **2017**, *100*, 26–30. [[CrossRef](#)]
17. Wang, J.; Yin, D.; Ma, J.; Liu, P.; Wang, Y.; Dong, Z.; Kong, L.B.; Tang, D. Pump laser induced photodarkening in ZrO₂-doped Yb:Y₂O₃ laser ceramics. *J. Eur. Ceram. Soc.* **2019**, *39*, 635–640. [[CrossRef](#)]
18. Gaume, R.; He, Y.; Markosyan, A.; Byer, R.L. Effect of Si-induced defects on 1 μm absorption losses in laser-grade YAG ceramics. *J. Appl. Phys.* **2012**, *111*, 093104. [[CrossRef](#)]
19. Fursikov, P.V.; Abdusalyamova, M.N.; Makhmudov, F.A.; Shairmardanov, E.N.; Kovalev, I.D.; Kovalev, D.Y.; Morgunov, R.B.; Koplak, O.V.; Volodin, A.A.; Khodos, I.I.; et al. Structural features and magnetic behavior of nanocrystalline powders of terbium oxide prepared by the thermal decomposition of terbium acetate in air. *J. Alloys Compd.* **2016**, *657*, 163–173. [[CrossRef](#)]
20. Kai, F.; Bin, L.; Hongmei, C.; Shaofan, W.; Yan, W.; Yongxing, L. Synthesis of ultrafine TbO_{1.81} and Tb₂O₃ powders for magneto-optical application. *J. Synth. Cryst.* **2021**, *50*, 80–87.
21. Abu-Zied, B.M.; Mohamed, A.-R.N.; Asiri, A.M. Effect of thermal treatment on the formation, textural and electrical conductivity properties of nanocrystalline Tb₄O₇. *J. Nanosci. Nanotechnol.* **2015**, *15*, 4487–4492. [[CrossRef](#)]
22. Kurland, H.-D.; Grabow, J.; Stotzel, C.; Muller, F.A. Preparation of ceramic nanoparticles by CO₂ laser vaporization. *J. Ceram. Sci. Technol.* **2014**, *5*, 275–280.
23. Osipov, V.V.; Platonov, V.V.; Lisenkov, V.V.; Tikhonov, E.V.; Podkin, A.V. Study of nanoparticle production from yttrium oxide by pulse-periodic radiation of ytterbium fibre laser. *Appl. Phys. A* **2018**, *124*, 3. [[CrossRef](#)]
24. Maksimov, R.N.; Shitov, V.A.; Platonov, V.V.; Yurovskikh, A.S.; Toci, G.; Patrizi, B.; Vannini, M.; Pirri, A. Hot isostatic pressing of transparent Yb³⁺-doped Lu₂O₃ ceramics for laser applications. *Ceram. Int.* **2021**, *47*, 5168–5176. [[CrossRef](#)]
25. Baenziger, N.C.; Eick, H.A.; Schuldt, H.S.; Eyring, L. Terbium oxides. III. X-ray diffraction studies of several stable phases. *J. Am. Chem. Soc.* **1961**, *83*, 2219–2223. [[CrossRef](#)]
26. MacChesney, J.B.; Williams, H.J.; Sherwood, R.C.; Potter, J.F. Preparation and low-temperature magnetic properties of the terbium oxides. *J. Chem. Phys.* **1966**, *44*, 596–601. [[CrossRef](#)]
27. Velazquez, M.; Pechev, S.; Duttine, M.; Wattiaux, A.; Labrugere, C.; Veber, P.; Buffiere, S.; Denux, D. Point defect disorder in high-temperature solution grown Sr₆Tb_{0.94}Fe_{1.06}(BO₃)₆ single crystals. *J. Solid State Chem.* **2018**, *264*, 91–97. [[CrossRef](#)]
28. Sarma, D.D.; Rao, C.N.R. XPS studies of oxides of second- and third-row transition metals including rare earth. *J. Electron Spectrosc. Relat. Phenom.* **1980**, *20*, 25–45. [[CrossRef](#)]
29. Blanco, G.; Pintado, J.M.; Bernal, S.; Cauqui, M.A.; Corchado, M.P.; Galtayries, A.; Ghijsen, J.; Sporcken, R.; Eickhoff, T.; Drube, W. Influence of the nature of the noble metal (Rh,Pt) on the low-temperature reducibility of a Ce/Tb mixed oxide with application as TWC component. *Surf. Interface Anal.* **2002**, *34*, 120–124. [[CrossRef](#)]
30. Glatzle, M.; Janka, O.; Svitlyk, V.; Chernyshov, D.; Bartsch, M.; Zacharias, H.; Pottgen, R.; Huppertz, H. The high-pressure oxide Tb₃O₅ and its non-centrosymmetric low-temperature polymorph—A comprehensive study. *Chem. Eur. J.* **2018**, *24*, 15236–15245. [[CrossRef](#)]
31. Wu, Y.; Shi, C. Observation of Eu²⁺ and Tb⁴⁺ in SrMgF₄:Eu³⁺, Tb³⁺. *Solid State Commun.* **1995**, *95*, 319–322. [[CrossRef](#)]

32. Van den Bossche, J.; Neyts, K.A.; De Visschere, P.; Corlatan, D.; Pauwels, H.; Vercaemst, R.; Fiermans, L.; Poelman, D.; Van Meirhaeghe, R.L.; Lafrele, W.H.; et al. XPS Study of TbF₃ and TbOF Centres in ZnS. *Phys. Status Solidi A* **1994**, *146*, K67–K70. [[CrossRef](#)]
33. Mugiraneza, S.; Hallas, A.M. Tutorial: A beginner's guide to interpreting magnetic susceptibility data with the Curie-Weiss law. *Commun. Phys.* **2022**, *5*, 95. [[CrossRef](#)]
34. Vickery, R.C.; Ruben, A. Magnetic susceptibilities of praseodymium and terbium oxides. *J. Chem. Soc.* **1959**, 510–513. [[CrossRef](#)]
35. Balabanov, S.S.; Permin, D.A.; Rostokina, E.Y.; Egorov, S.V.; Sorokin, A.A. Sinterability of nanopowders of terbium solid solutions with scandia, yttria, and lutetia. *J. Adv. Ceram.* **2018**, *7*, 362–369. [[CrossRef](#)]
36. Ikesue, A.; Aung, Y.L.; Lupei, V. *Ceramic Lasers*; Cambridge University Press: Cambridge, UK, 2013; p. 152.
37. Biswas, P.; Chakravarty, D.; Suresh, M.B.; Johnson, R.; Mohan, M.K. Fabrication of graphite contamination free polycrystalline transparent MgAl₂O₄ spinel by spark plasma sintering using platinum foil. *Ceram. Int.* **2016**, *42*, 18920–18923. [[CrossRef](#)]
38. Wang, P.; Yang, M.; Zhang, S.; Tu, R.; Goto, T.; Zhang, L. Suppression of carbon contamination in SPSe-d CaF₂ transparent ceramics by Mo foil. *J. Eur. Ceram. Soc.* **2017**, *37*, 4103–4107. [[CrossRef](#)]
39. Gan, L.; Park, Y.-J.; Park, M.-J.; Kim, H.; Kim, J.-M.; Ko, J.-W.; Lee, J.-W. Facile fabrication of highly transparent yttria ceramics with fine microstructures by a hot-pressing method. *J. Am. Ceram. Soc.* **2015**, *98*, 2002–2004. [[CrossRef](#)]
40. Chen, T.; Xu, Y.; Li, L.; Zhu, J.; Cong, M.; Song, J. Eliminate of colour center and growth of large-size Tb₃Ga₅O₁₂ crystals. *J. Cryst. Growth* **2021**, *562*, 126090. [[CrossRef](#)]
41. Ibanez, J.; Sans, J.A.; Cuenca-Gotor, V.; Oliva, R.; Gomis, O.; Rodríguez-Hernández, P.; Muñoz, A.; Rodríguez-Mendoza, U.; Velázquez, M.; Veber, P.; et al. Structural and lattice-dynamical properties of Tb₂O₃ under compression: A comparative study with rare earth and related sesquioxides. *Inorg. Chem.* **2020**, *59*, 9648–9666. [[CrossRef](#)]
42. Candela, M.T.; Aguado, F.; Gonzalez-Lavín, J.; Gonzalez, J.A.; Valiente, R. Modification of the spectroscopic properties of Tb₂O₃ phosphor under the high-pressure phase transitions sequence. *J. Alloys Compd.* **2021**, *859*, 157899. [[CrossRef](#)]
43. Gunasekaran, S.; Anbalagan, G.; Pandi, S. Raman and infrared spectra of carbonates of calcite structure. *J. Raman Spectrosc.* **2006**, *37*, 892–899. [[CrossRef](#)]
44. Slezak, O.; Yasuhara, R.; Lucianetti, A.; Mocek, T. Temperature-wavelength dependence of terbium gallium garnet ceramics Verdet constant. *Opt. Mater. Express* **2016**, *6*, 3683–3691. [[CrossRef](#)]